Supporting Information

Room-Temperature Lasing in Colloidal Nanoplatelets via Mie-Resonant Bound States in the Continuum

Mengfei Wu,[†,§] Son Tung Ha,[†,§] Sushant Shendre,[‡] Emek G. Durmusoglu,[‡] Weon-Kyu Koh,[‡] Diego R. Abujetas,[‖] José A. Sánchez-Gil,[‖] Ramón Paniagua-Domínguez,[†] Hilmi Volkan Demir,*[,‡,□] Arseniy I. Kuznetsov*[,†]

[†]Institute of Materials Research and Engineering, A*STAR (Agency for Science, Technology and Research), 138634, Singapore

[‡]LUMINOUS! Centre of Excellence for Semiconductor Lighting and Displays, Nanyang Technological University, 639798, Singapore

[‖]Instituto de Estructura de la Materia (IEM-CSIC), Consejo Superior de Investigaciones Científicas, 28006, Madrid, Spain

[□]UNAM-Institute of Materials Science and Nanotechnology, Bilkent University, 06800, Ankara, Turkey

[§]Contributed equally

*Corresponding authors: arseniy_kuznetsov@imre.a-star.edu.sg; hvdemir@ntu.edu.sg

METHODS

Synthesis of Colloidal Nanoplatelets

Cadmium oxide [CdO] (99.9%), cadmium acetate dihydrate [$Cd(OAc)_2 \cdot 2H_2O$] (>98%), zinc acetate [$Zn(OAc)_2$] (99.99%), myristic acid (>99%), 1-octadecene (ODE), selenium (Se) (99.99% trace metals basis), oleic acid (OA) (90%), oleylamine (OLA) (70%), 1-octanethiol (≥98.5%), hexane, and ethanol (EtOH) were purchased from Sigma Aldrich.

CdSe NPLs which are four monolayers in thickness were synthesized as follows (modified slightly from the literature method[1]): 77 mg of CdO and 340 mg of myristic acid were dissolved in 28 mL of ODE, and the solution was degassed at 100 °C. The temperature was increased to 285 °C under argon flow, and the solution was heated until it turned colourless. Then the solution was cooled to 90 °C for injection of 24 mg of Se powder dissolved in 2 mL of ODE. The temperature was then set to 235 °C. At 195 °C, 160 mg $Cd(OAc)_2 \cdot 2H_2O$ was added swiftly to initiate anisotropic growth. After 10 minutes of growth at 235 °C, the reaction was terminated with the addition of 1 mL OA and was cooled to room temperature by water bath. The CdSe NPL solution was diluted by addition of 5 mL of hexane and was washed by addition of EtOH followed by centrifugation at 6000 rpm. Precipitates were re-dispersed in hexane for further shell growth.

To synthesize CdSe/CdZnS core-shell NPLs, we modified the literature method[2] slightly. 11.53 mg of $Cd(OAc)_2 \cdot 2H_2O$, 27.52 mg of $Zn(OAc)_2$, and 0.5 mL of OA in 5 mL of ODE were degassed under vacuum at 80 °C for 60 min, followed by additional degassing under argon at 200 °C for 10 min. Once the solution was cooled to 80 °C, 1 mL of the 4-monolayer CdSe core NPLs in hexane was added and degassed for another 30 min. Then under argon flow, the temperature of the solution

was set to 300 °C. Degassed OLA (0.5 mL) was injected at 90 °C. 1-octanethiol (70 μL) in 4 mL of ODE was injected at 165 °C at a rate of 10 mL/h with a syringe pump. The injection rate was decreased to 4 mL/h when the temperature of the solution reached 240 °C. When the temperature reached 300 °C, the solution was kept at this temperature for 50 min. CdSe/CdZnS NPLs were washed by addition of EtOH and centrifugation at 6000 rpm and re-dispersed in hexane.

Fabrication of Dielectric Nanostructures

Fused silica (quartz) substrates were cleaned by ultra-sonication in deionised (DI) water, acetone, and isopropanol. A 120 nm-thick film of TiO_2 was deposited by ion-assisted sputtering (Oxford Optofab3000). Then a 30 nm-thick film of chromium (Cr) was deposited by electron-beam (e-beam) evaporation (Angstrom EvoVac). For patterning, a negative electron-beam resist, hydrogen silsesquioxane (HSQ, Dow Corning XR-1541-006) was spin-cast on the TiO_2-Cr-coated substrate at 5000 rpm for 60 seconds, followed by baking at 140 °C for 3 minutes. This led to a HSQ film thickness of about 120 nm. We found that heating the substrate at 140 °C for 1 min before spin-coating HSQ improved adhesion of HSQ on Cr. The sample then underwent e-beam lithography (Elionix ELS-7000), after which HSQ was developed by immersion in a salty developer[3] (1 wt.% NaOH and 4 wt.% NaCl in DI water) for 4 minutes, followed by a generous rinse in DI water. Using inductively coupled plasma reactive ion etching (ICP-RIE, Oxford PlasmaPro 100 Cobra), the pattern in HSQ, i.e. arrays of nanopillars, was first transferred to the Cr layer with a mixture of Cl_2 and O_2 gases (Cl2: 19 sccm, O2: 2 sccm, 10 mTorr). Then, using Cr as a hard mask (since HSQ is etched together with TiO_2), the pattern was transferred to the TiO_2 layer with CHF_3 gas (25 sccm, 25 mTorr). Finally, Cr together with any residual HSQ were removed by immersing the

sample in liquid chromium etchant (Sigma Aldrich) for 4 minutes. The sample was rinsed in water and IPA and blown dry with nitrogen gas.

Deposition of Nanoplatelets

The substrate patterned with TiO_2 nanostructures was cleaned with isopropanol, blown dry, and subsequently treated with O_2 plasma for 2 minutes. The cleaned substrate was spin-coated in air with 10 μL of a highly concentrated (~50 mg/mL) solution of CdSe/CdZnS core-shell NPLs in hexane in a two-speed process: starting at 500 rpm, followed by 4000 rpm for 30 seconds. This was immediately followed by spin-rinsing the deposited NPLs with 50 μL of pure ethanol at 2000 rpm for 30 seconds. The sample was then stored in a glovebox and covered with a piece of polydimethylsiloxane (PDMS, ~ 0.1 mm thick) before optical characterization under ambient conditions.

Optical Characterization

Optical characterization was performed with an inverted optical microscope (Nikon Ti-U) coupled to a spectrometer (Andor SR-303i) equipped with an electron-multiplying charged-coupled detector (EMCCD, Andor Newton 971). For reflectance measurements, light from a halogen lamp passing through a linear polarizer was focused onto the sample surface via a 50× objective (NA = 0.55). The reflected light was collected with the same objective and passed through a series of lenses, which imaged the back focal plane (BFP) of the objective onto the entrance slit of the spectrometer. The slit width was set to 100 μm to capture a thin slice of the BFP image, corresponding to light reflected from the sample in the *y*-*z* plane only. A grating with groove

density of 150 g/mm was used to disperse the wavelengths. The CCD in the spectrometer then gave a reflectance spectrum resolved in both wavelength and angle of reflection in the *y*-*z* plane.

For photoluminescence (PL) measurements, light from a continuous-wave laser at $\lambda = 488$ nm was focused onto the sample via a 50× objective (NA = 0.55), and PL from the sample was collected through the same objective. For lasing measurements, the input laser is pulsed at $\lambda = 530$ nm with 200 fs pulse width at a repetition rate of 20 kHz. It was focused onto the sample via a top 2× objective (NA = 0.15) so that the spot size was approximately 60 μm to illuminate a single 50 × 50 μm cylinder array completely. Radiation from the sample was collected with a bottom 50× objective (NA = 0.55). In both cases, light collected was passed through an appropriate long-pass filter, a linear polarizer (when applicable), and the same lens system as in the reflectance measurements to image the BFP of the objective, i.e. the far-field radiation pattern of the sample. To record the entire BFP image, the spectrometer slit was fully opened (width = 2.5 mm), and grating was set to the zero order. The slit width was then adjusted to 100 μm and grating set to a centre wavelength of 650 nm to measure the angle-resolved PL spectra in the *y*-*z* plane of the sample. The groove density of the grating was 150 g/mm for PL measurements, and 1200 g/mm for lasing characterization.

Numerical Simulation

Simulations were carried out using the Finite Element Method (Comsol Multiphysics v5.5). For that, a single unit cell was simulated and Bloch boundary conditions applied in the lateral directions, to mimic an infinitely extended system. This system was excited, and the reflection and transmission recorded, using a set of periodic ports (one for each diffraction order supported by

the system in the studied angular and wavelength span). The material parameters of TiO_2 were taken from ellipsometry measurements, which closely reproduced those reported in literature,[4] and the external medium was considered homogeneous with refractive index 1.46, thus representing the quartz substrate and the index-matching PDMS cover used in the experiments.

To identify the character of the different multipolar resonances supported by the system, we employed the multipole decomposition technique. In this case, we used the decomposition based on the scattering current density induced in the particles by the incident field,[5] which takes the form of (assuming a $e^{-i\omega t}$ temporal dependence, ω being the angular frequency of the wave):

$$\boldsymbol{J} = -i\omega\varepsilon_0(\varepsilon - \varepsilon_d)\boldsymbol{E}$$

where ε_0 is the permittivity of vacuum, ε_d and ε, respectively, the relative permittivities of the surrounding medium and the particle, and $\boldsymbol{E} = \boldsymbol{E}(\boldsymbol{r})$ the electric field. By decomposing this scattering current density into different multipolar contributions, it is possible to identify the character of the resonances excited in the system. This can be done using a spherical basis[5] or a Cartesian one,[6] the latter being the one used in this work. In this basis, the different electric and magnetic multipolar moments (up to the quadrupolar order) can be written in terms of the scattering current density as:

$$\text{electric dipole (ED) moment} \rightarrow \boldsymbol{p} = \frac{i}{\omega}\int \boldsymbol{J} d\boldsymbol{r},$$

$$\text{magnetic dipole (MD) moment} \rightarrow \boldsymbol{m} = \frac{1}{2}\int [\boldsymbol{r} \times \boldsymbol{J}] d\boldsymbol{r},$$

$$\text{electric quadrupole (EQ) moment} \rightarrow \overline{\overline{\boldsymbol{Q}}}_{\boldsymbol{e}} = \frac{i}{\omega}\int [\boldsymbol{r}\otimes\boldsymbol{J} + \boldsymbol{J}\otimes\boldsymbol{r}] d\boldsymbol{r},$$

$$\text{magnetic quadrupole (MQ) moment} \rightarrow \overline{\overline{\boldsymbol{Q}}}_{\boldsymbol{m}} = \frac{1}{3}\int [\boldsymbol{r}\otimes(\boldsymbol{r} \times \boldsymbol{J}) + (\boldsymbol{r} \times \boldsymbol{J})\otimes\boldsymbol{r}] d\boldsymbol{r}.$$

In these expressions, $\otimes$ represents the outer product. Once the multipolar moments are known, one can compute the contribution to the scattering cross section associated with a particular multipole component as:

$$C_{sca}{}^{(ED_i)} = \frac{k_0^4}{6\pi\varepsilon_0^2 E_0^2}|p_i|^2$$

$$C_{sca}{}^{(MD_i)} = \frac{\eta_0^2\varepsilon_d k_0^4}{6\pi E_0^2}|m_i|^2$$

$$C_{sca}{}^{(EQ_{ij})} = \frac{\varepsilon_d k_0^6}{80\pi\varepsilon_0^2 E_0^2}|\overline{\overline{Q}}_{e,\,ij}|^2$$

$$C_{sca}{}^{(MQ_{ij})} = \frac{\eta_0^2\varepsilon_d^2 k_0^6}{80\pi n_d E_0^2}|\overline{\overline{Q}}_{m,ij}|^2$$

where $i,j = x,y,z$. Then, the scattering cross section for each multipole can be simply computed by summing over its components and the total one summing over multipoles.

The near fields were recorded at an angle of incidence of 0.5°. The emission pattern of the array was computed using reciprocal calculations, by which the system was excited from the far field using planes waves at different angles and both polarizations, and the field intensity integrated in the volume around the structures.[7]

REFERENCES

(1) Antanovich, A.; Prudnikau, A.; Matsukovich, A.; Achtstein, A.; Artemyev, M. Self-Assembly of CdSe Nanoplatelets into Stacks of Controlled Size Induced by Ligand Exchange. *J. Phys. Chem. C* **2016**, *120*, 5764–5775.

(2) Altintas, Y.; Gungor, K.; Gao, Y.; Sak, M.; Quliyeva, U.; Bappi, G.; Mutlugun, E.; Sargent, E. H.; Demir, H. V. Giant Alloyed Hot Injection Shells Enable Ultralow Optical Gain Threshold in Colloidal Quantum Wells. *ACS Nano* **2019**, *13*, 10662–10670.

(3) Yang, J. K. W.; Berggren, K. K. Using High-Contrast Salty Development of Hydrogen Silsesquioxane for Sub-10-Nm Half-Pitch Lithography. *J. Vac. Sci. Technol. B* **2007**, *25*, 2025–2029.

(4) *Handbook of Optical Constants of Solids*; Palik, E. D., Ed.; Academic Press, 1997.

(5) Grahn, P.; Shevchenko, A.; Kaivola, M. Electromagnetic Multipole Theory for Optical Nanomaterials. *New J. Phys.* **2012**, *14*, 093033.

(6) Paniagua-Domínguez, R.; Yu, Y. F.; Miroshnichenko, A. E.; Krivitsky, L. A.; Fu, Y. H.; Valuckas, V.; Gonzaga, L.; Toh, Y. T.; Kay, A. Y. S.; Lukyanchuk, B.; et al. Generalized Brewster Effect in Dielectric Metasurfaces. *Nat. Commun.* **2016**, *7*, 10362.

(7) Khaidarov, E.; Liu, Z.; Paniagua-Domínguez, R.; Ha, S. T.; Valuckas, V.; Liang, X.; Akimov, Y.; Bai, P.; Png, C. E.; Demir, H. V.; et al. Control of LED Emission with Functional Dielectric Metasurfaces. *Laser Photonics Rev.* **2020**, *14*, 1900235.

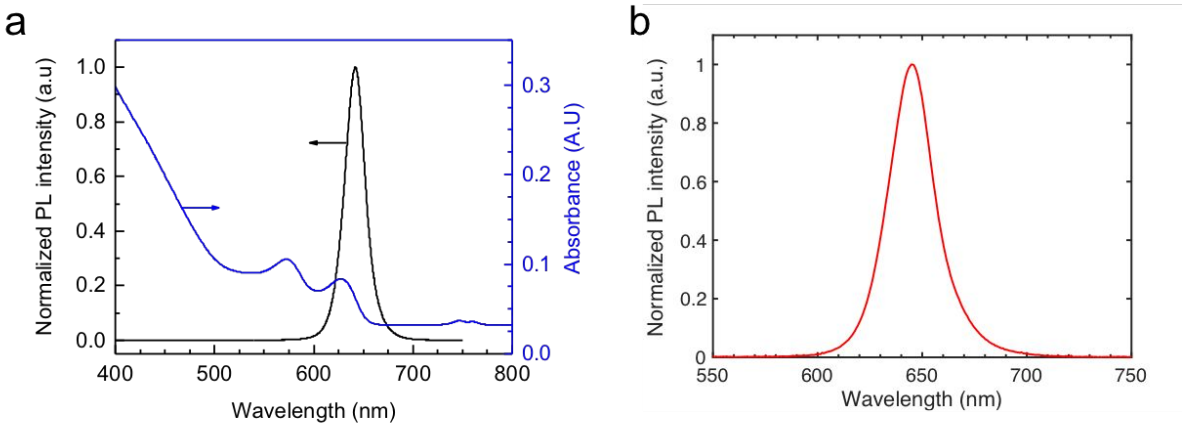

Figure S1. (a) Absorption and photoluminescence (PL) spectra of CdSe/CdZnS core-shell nanoplatelets (NPLs) dissolved in hexane. The first excitonic absorption peak is measured at λ = 629 nm, while PL peaks at λ = 642 nm with a full width at half maximum (FWHM) of 24 nm when the solution is excited at λ = 380 nm. (b) In a spin-cast film of NPLs, the PL peak is slightly red-shifted to λ = 645 nm with a FWHM = 25 nm, when excited at λ = 488 nm.

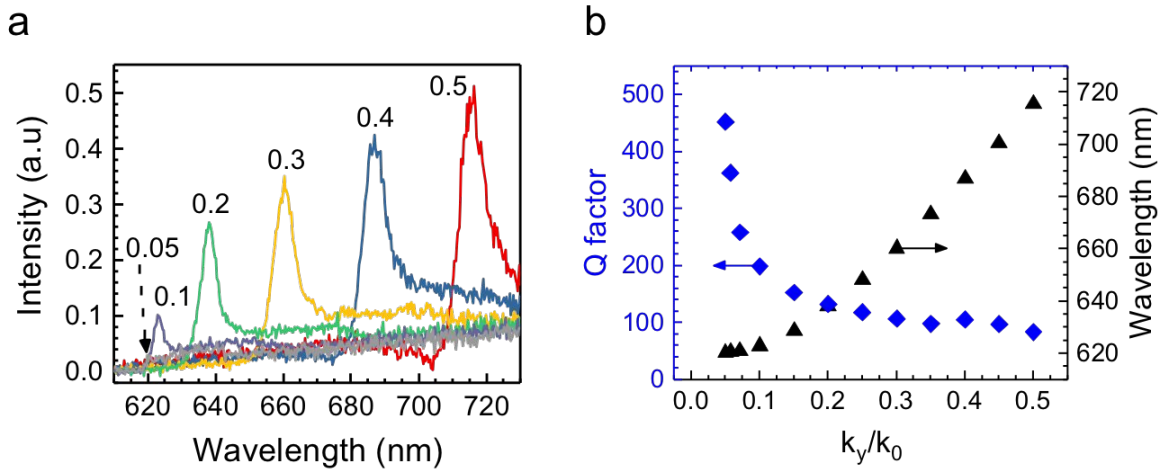

Figure S2. (a) Reflectance spectra extracted from Figure 2a at various angles of incidence (reflection), labeled by the in-plane momentum k_y/k_0. (b) Angular dependence of the Q factor and resonant wavelength of the mode associated with out-of-plane magnetic dipoles, derived from the spectra in (a). Characteristic of symmetry-protected bound states in the continuum (BICs), the Q factor increases dramatically as the angle of incidence approaches zero, reaching approximately 450 at $k_y/k_0 = 0.05$ ($\theta = 2.9°$). Resonances with higher Q factors closer to the BIC condition cannot be resolved, as the measurement setup has a spectral resolution of ~ 1 nm.

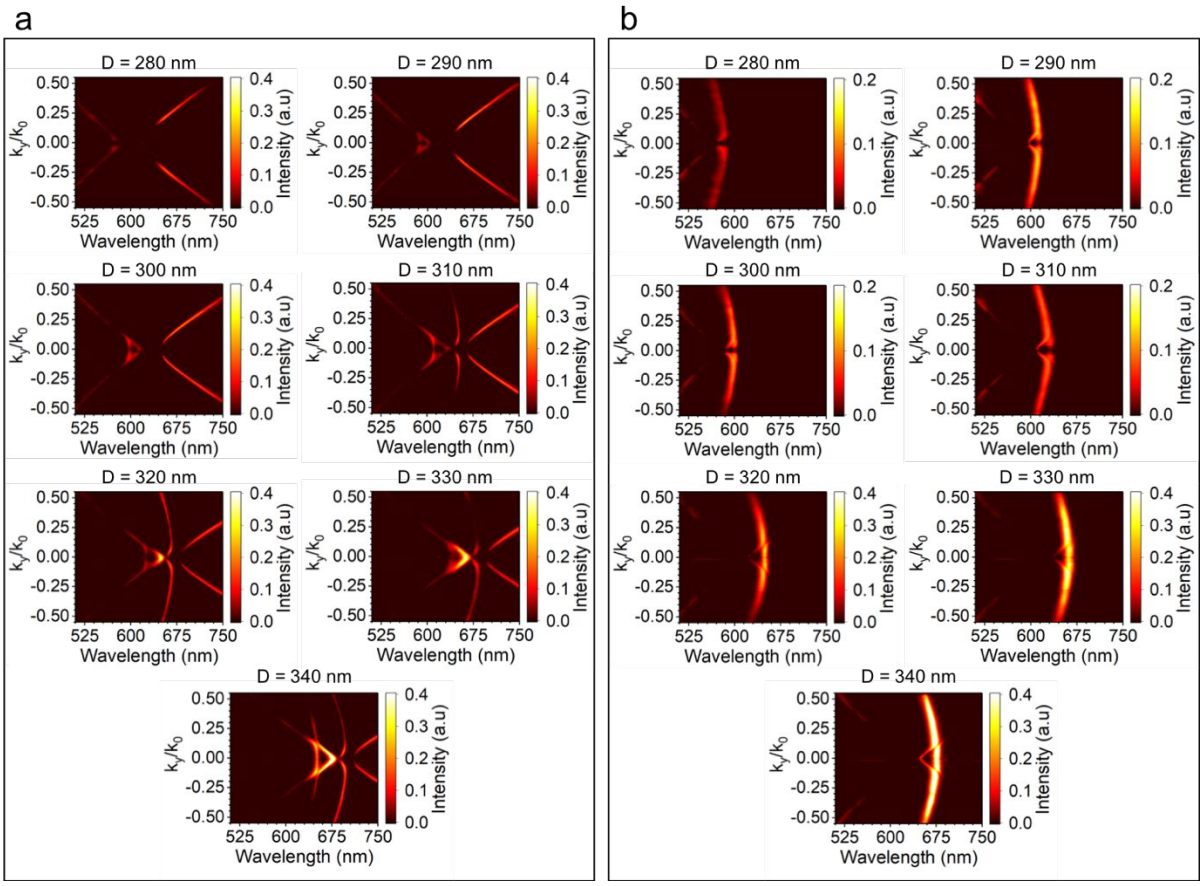

Figure S3. Angle-resolved reflectance spectra of arrays of TiO_2 cylinders coated *with* nanoplatelets (NPLs), for various cylinder diameters *D* as marked, under incident light of (a) transverse electric, TE and (b) transverse magnetic, TM polarizations. The range of angles of reflection (± 33°) is defined by the objective with NA = 0.55 used in the measurements. Some of the features observed in the reflectance spectra of arrays *without* NPLs (Figures 2a, b), particularly in the bluer wavelengths, are missing due to absorption in NPLs. The bound state in the continuum (BIC) based on out-of-plane magnetic dipoles is still visible, e.g. at $\lambda \sim 650$ nm for $D = 300$ nm under TE polarization.

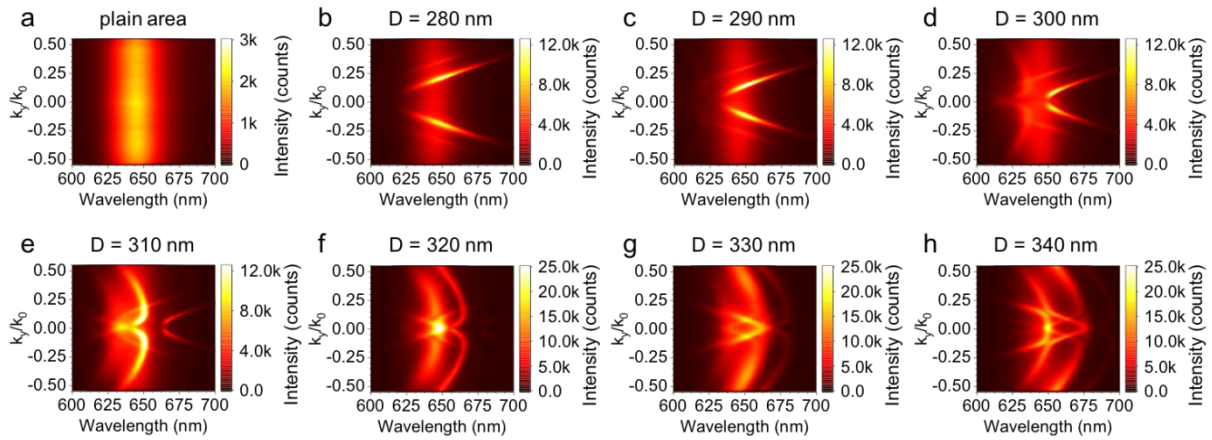

Figure S4. Angle-resolved photoluminescence (PL) spectra of nanoplatelets on (a) a plain area of the substrate, and (b-h) arrays of TiO_2 cylinders with various diameters: D = 280 to 340 nm. The angle of emission in the y-z plane is denoted by the ratio between the projected in-plane momentum k_y and free-space momentum k_0. PL is coupled to different modes as the bands red-shift with increasing D. The sample is excited at λ = 488 nm with a continuous-wave (CW) laser, and PL is collected without a polarizer.

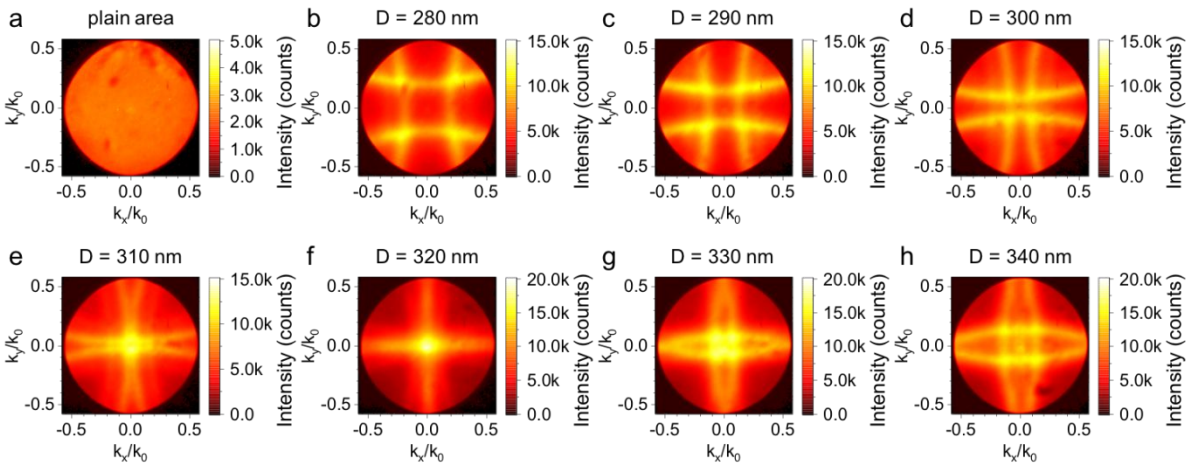

Figure S5. Images of the back focal plane, showing the far-field radiation pattern of the nanoplatelets on (a) a plain area of the substrate, and (b-h) arrays of TiO_2 cylinders with various diameters: $D = 280$ to 340 nm. Arcs of four circles (centred on the $\pm$ x and y axes), which correspond to the diffraction bands of the photoluminescence (PL), approach $k_x = k_y = 0$ as the period of the array increases, and eventually pass the origin as the lattice turns from sub-diffractive to diffractive for in-phase multipoles around $D = 320$ nm. The sample is excited at $\lambda = 488$ nm with a CW laser, and PL is collected without a polarizer.

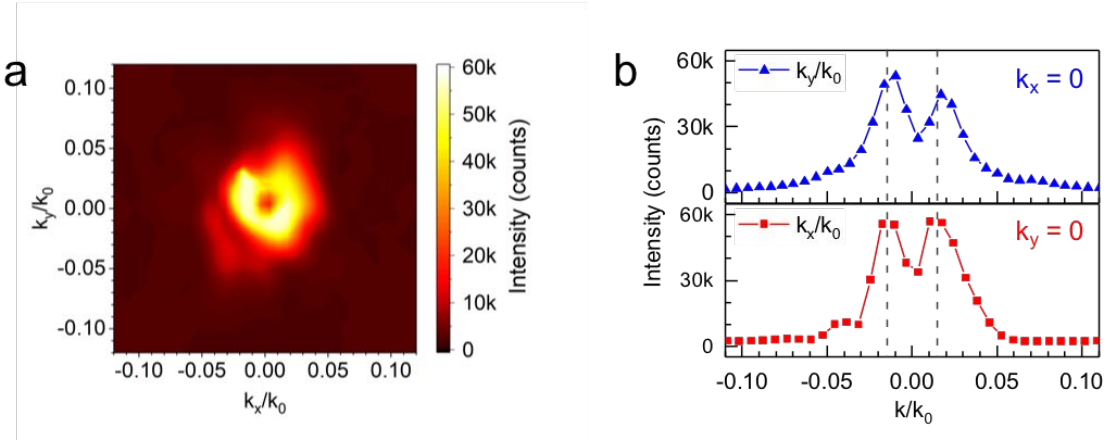

Figure S6. (a) Far-field radiation pattern during lasing for an array of TiO_2 cylinders with diameter D = 300 nm. This is a zoomed-in view of Figure 3e. The doughnut shape in the normal direction confirms that lasing arises from a bound state in the continuum (BIC). (b) Line scans along the y (blue) and x (red) axes of (a), showing the angle-resolved lasing intensity. Although the BIC is in theory decoupled from the radiation field, the intensity at $k_x = k_y = 0$ is finite due to sample imperfections (e.g. finite size, scattering). Peaks in lasing intensity are observed at $k_{\|}/k_0 = \pm 0.014$, corresponding to an angle of ~ 0.8° into the free space, or ~ 0.5° in the active layer with an index of 1.7.

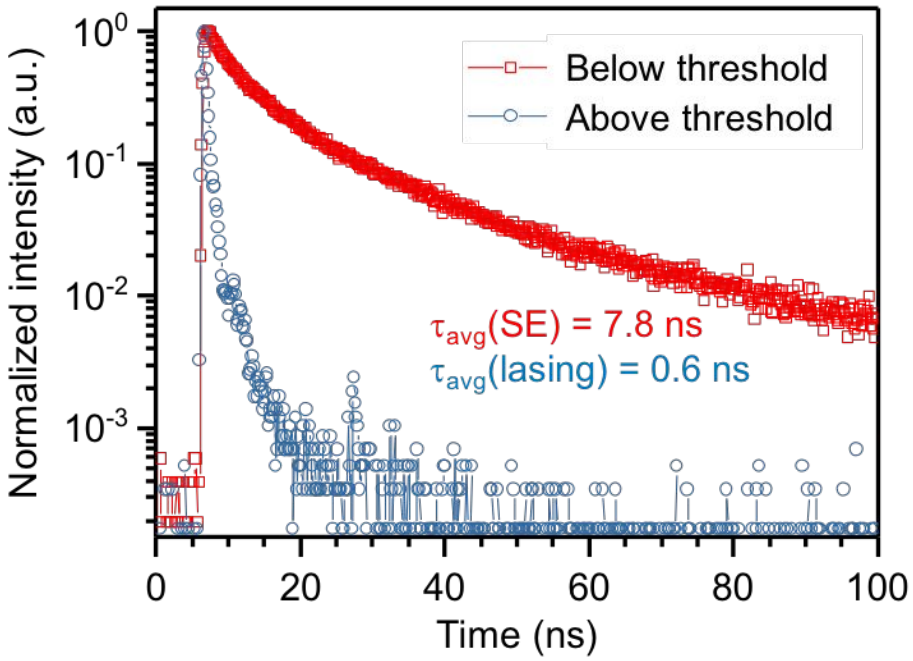

Figure S7. Time-resolved photoluminescence (PL) of nanoplatelets on an array of TiO_2 cylinders with diameter $D = 300$ nm when the pump fluence is below (red) and above (blue) the lasing threshold. τ_{avg}: PL lifetime as a weighted average of the time constants in a bi-exponential fit. SE: spontaneous emission.

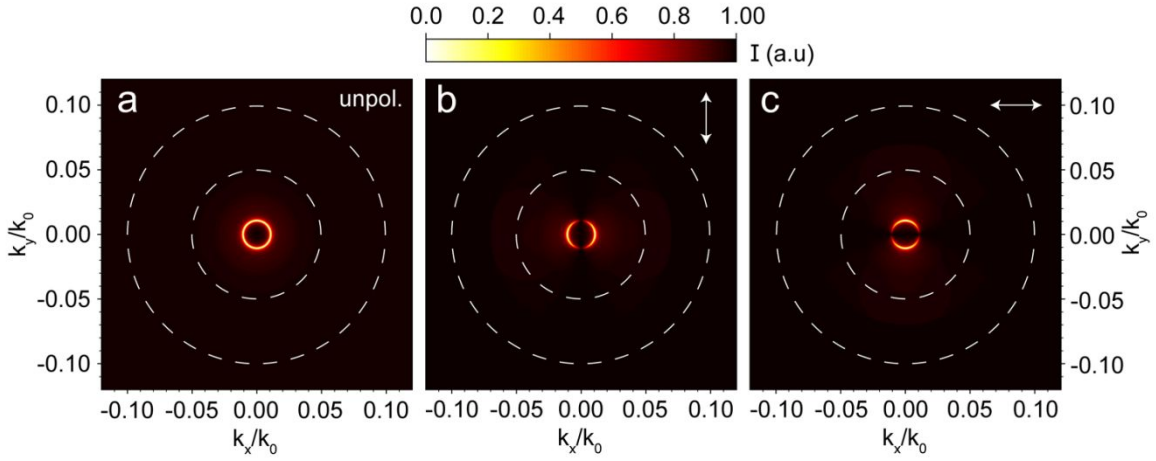

Figure S8. (a–c) Numerically calculated far-field radiation pattern near the normal direction for a BIC comprising out-of-plane magnetic dipoles, using reciprocal calculations (see Methods): (a) unpolarized emission; (b,c) in the presence of a linear polarizer in the direction marked by the white arrow. The simulated polarization dependence suggests that the BIC inherits the TE-polarized radiation pattern of the constituent *z*-oriented magnetic dipoles.

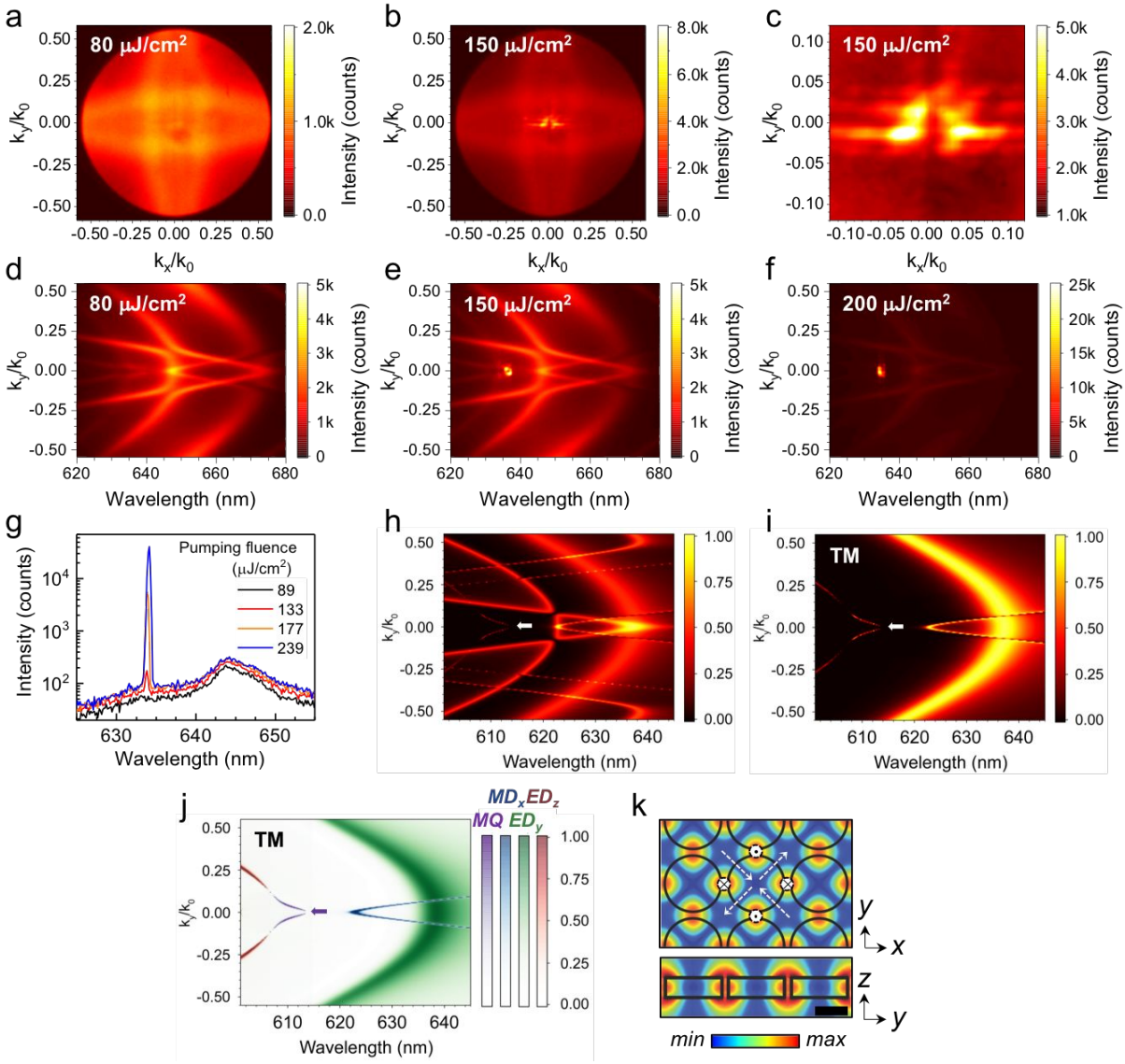

Figure S9. (a–c) Back focal plane (BFP) images of the nanoplatelet (NPL) photoluminescence (PL) on an array of TiO_2 cylinders with diameter D = 340 nm. The array is excited with a pulsed laser at λ = 530 nm at a fluence (a) below and (b,c) just above the lasing threshold. (c) is a zoomed-in view of (b) at the centre of the BFP. The four lobes with nodes along x, y and z directions suggest that lasing arises from a BIC based on quadrupoles. (d–f) Angle-resolved PL spectra at pump fluences (d) below, (e) just above, and (f) well above the lasing threshold. The PL collected reflects modes of both TE and TM polarizations with respect to the y-z plane. (g) PL spectra at several

pump fluences, showing the onset of lasing. (h,i) Numerical simulations of the reflectance of the same array *without* NPLs under (h) unpolarized and (i) TM-polarized light. A BIC is observed at $\lambda = 614$ nm, marked by an arrow. (h) agrees well with the unpolarized PL (d,e). The modes are red-shifted in the PL due to the presence of higher-index NPLs. (j) Multipolar decomposition showing various Mie modes under TM polarization: electric dipoles (ED_y, ED_z), magnetic dipole (MD_x), and magnetic quadrupole (MQ). The BIC marked by an arrow originates from in-phase MQs. (k) Electric-field intensity in the cylinder array ($D = 340$ nm), corresponding to the MQ-BIC mode ($\lambda = 614$ nm). The MQ is formed by four loops of displacement current circulating perpendicular to the lattice plane. Top: *x*-*y* plane cut at half height; bottom: *y*-*z* plane cut along the cylinder diameter. The TiO_2 cylinders are outlined in black. The directions of electric and magnetic fields are indicated with black and white dashed arrows, respectively. Black scale bar: 200 nm.